Phase-locking flows between orthogonally stretching parallel plates

B. Wang,[1] R. Ayats,[1] A. Meseguer,[1] and F. Marques[1]

Department of Physics, Universitat Politècnica de Catalunya, Barcelona 08034, Spain

(Dated: 23 October 2022)

In this paper we explore the stability and dynamical relevance of a wide variety of steady, time-periodic, quasiperiodic and chaotic flows arising between orthogonally stretching parallel plates. We first explore the stability of all the steady flow solution families formerly identified by Ayats *et al.* [Ayats, R., Marques, F., Meseguer, A. and Weidman, P., *Flows between orthogonally stretching parallel plates*, Phys. Fluids, **33**, 024103 (2021)], concluding that only the one that originates from the Stokesian approximation is actually stable. When both plates are shrinking at identical or nearly the same deceleration rates, this Stokesian flow exhibits a Hopf bifurcation that leads to stable time-periodic regimes. The resulting time-periodic orbits or flows are tracked for different Reynolds numbers and stretching rates, whilst monitoring their Floquet exponents to identify secondary instabilities. It is found that these time-periodic flows also exhibit Neimark-Sacker bifurcations, generating stable quasiperiodic flows (tori) that may sometimes give rise to chaotic dynamics through a Ruelle-Takens-Newhouse scenario. However, chaotic dynamics is unusually observed, as the quasiperiodic flows generally become *phase-locked* through a *resonance* mechanism before a strange attractor may arise, thus restoring the time-periodicity of the flow. In this work we have identified and tracked four different resonance regions, also known as *Arnold tongues* or *horns*. In particular, the $1:4$ strong resonance region is explored in great detail, where the identified scenarios are in very good agreement with normal form theory.

I. INTRODUCTION

The motion of wall-bounded viscous fluids induced by stretching or shrinking of their boundaries are of interest in many areas of science and technology such as cooling and extrusion processes, paper production, polymer processing and metallurgy (Aziz and Mahomed, 2016; Merkin and Pop, 2018). Furthermore, these type of flows can be used to mathematically model certain physiological processes arising in cardiology (Waters, 2001, 2004). The mathematical formulation of these type of flows usually assumes self-similarity of the Navier-Stokes solution, incorporating in it the spatial dependence of the non-uniform boundary conditions at the stretching or shrinking walls. We refer the reader to the monograph by Drazin and Riley (2006) for an extensive review of exact Navier-Stokes solutions, including self-similar profiles, and to Wang (2011) for unbounded flows induced by extended stretching boundaries.

Fluid motion induced by a single stretching flat plate, whose velocity is proportional to the distance from the stagnation point, was first studied by Crane (1970). The three-dimensional generalization of this problem, consisting of a biorthogonally stretching membrane, was later addressed in Wang (1984) and more recently in Weidman and Ishak (2015). Whereas in Crane's original formulation it is assumed that the wall-normal coordinate is unbounded, later studies have explored flows arising in two-dimensional channels with confining parallel walls stretching and shrinking in the streamwise direction (Brady and Acrivos, 1981; Marques *et al.*, 2017). For moderate Reynolds numbers, alternative formulations (Espín and Papageorgiou, 2009) that do not assume self-similarity of the flow have provided dynamics which are consistent with self-similar computations.

In Ayats *et al.* (2021) the generalized problem of a viscous fluid confined between two orthogonally stretching-shrinking parallel plates was studied numerically. In that work, five different families of steady self-similar flows were identified and explored for a wide range of independent orthogonal acceleration rates of the two walls. However, the dynamical relevance of these solutions remained unclear. In the present work, we first aim at exploring the stability of the aforementioned solution families and identifying their potential bifurcations that may lead to dynamically stable time-dependent flows. This is mainly motivated by the fact that flows arising within two-dimensional shrinking plates have been reported to exhibit a rich variety of complex dynamics, such as time-periodic regimes that become chaotic through period-doubling cascades (Marques *et al.*, 2017), for example. The emergence of complex flow dynamics when the walls bounding the fluid are shrinking has also been reported in non-cartesian geometries. This is the case for fluids confined within elastic cylindrical pipes when the pipe wall is contracting in the axial direction, with mild or absent azimuthal twist (Marques and Meseguer, 2019).

The paper is structured as follows. Section §II is devoted to the mathematical formulation of the problem, where the Navier-Stokes equations under the self-similar assumption are obtained for arbitrary time-dependent flows. The numerical methodologies are described in §III, where special emphasis is given to the adaptation of these methods for the linear stability analysis of steady flows, as well as to the computation of oscillatory flows and their Floquet analysis. The bifurcation mechanisms that give rise to oscillatory flows are presented in section §IV, identifying the parameter region where these stable time-periodic regimes may appear, and providing a detailed description of their dynamical properties and symmetries, in particular when both plates contract at the same deceleration rate. The stability of the oscillatory flows described in §IV is later on addressed in section §V, where the Neimark-Sacker bifurcation boundary is provided. This section also describes the bifurcated quasiperiodic and chaotic flows that are discussed in detail in section §VI, where the phase-locking regions are disclosed. This latter section devotes special attention to the $1:4$ strong resonance scenario. Finally, section §VII summarizes the main findings of the current exploration.

II. MATHEMATICAL FORMULATION

In this section we closely follow Ayats *et al.* (2021), summarizing the formulation and adding explicitly the time dependence, necessary for the linear stability analysis and computation of time dependent solutions.

We consider a viscous fluid of kinematic viscosity ν and density ρ confined between two infinite parallel plates, located at the *wall-normal* coordinates $z^* = \pm h$, as depicted in Fig. 1(a). The problem is formulated in Cartesian coordinates (x^*, y^*, z^*), where starred variables henceforth stand for dimensional quantities. In this coordinate system, $\mathbf{u}^* = (u^*, v^*, w^*)$ is the velocity field describing the motion of the fluid. The lower and upper plates linearly stretch along the x^* and y^* coordinates, respectively, so that the fluid velocities at those impermeable boundaries are

$$u^*(x^*, y^*, -h) = ax^*, \qquad v^*(x^*, y^*, -h) = 0, \qquad w^*(x^*, y^*, -h) = 0, \tag{1}$$

$$u^*(x^*, y^*, h) = 0, \qquad v^*(x^*, y^*, h) = by^*, \qquad w^*(x^*, y^*, h) = 0, \tag{2}$$

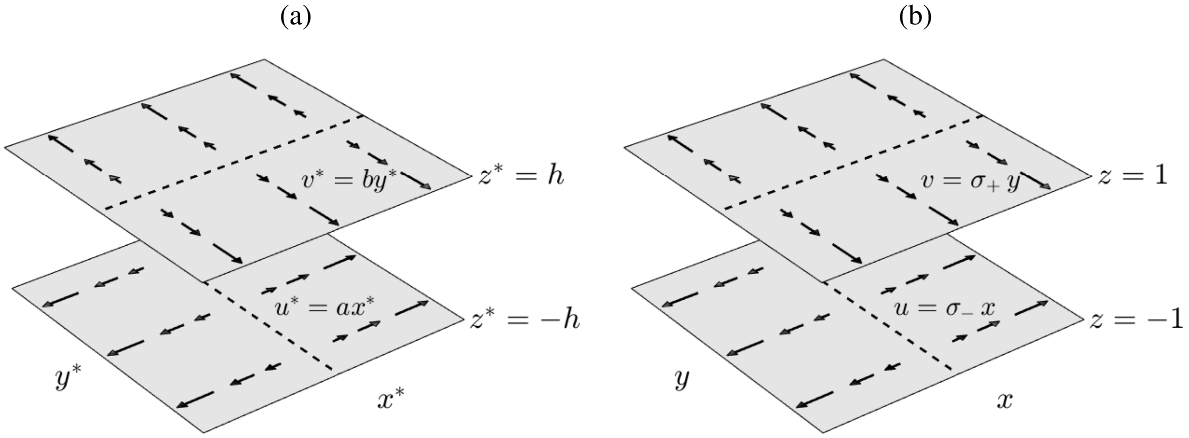

FIG. 1. Schematics of the problem. (a) In dimensional form. (b) Using non-dimensional variables. From Ayats *et al.* (2021) with permission of the publisher.

where a and b are the strain rate of stretching along the x^* and y^*-axis respectively.

The problem is rendered nondimensional after using h, h^2/ν, ν/h and $\rho\nu^2/h^2$ as units of length, time, velocity, and pressure, respectively, leading to the dimensionless incompressible Navier-Stokes equations

$$\nabla\cdot\mathbf{u} = 0, \qquad \partial_t\mathbf{u} + (\mathbf{u}\cdot\nabla)\mathbf{u} = -\nabla p + \nabla^2\mathbf{u}. \tag{3}$$

The boundary conditions in dimensionless coordinates read

$$u(x,y,-1) = \frac{ah^2}{\nu}x \equiv \sigma_- x, \quad v(x,y,-1) = 0, \quad w(x,y,-1) = 0, \tag{4}$$

$$u(x,y,1) = 0, \quad v(x,y,1) = \frac{bh^2}{\nu}y \equiv \sigma_+ y, \quad w(x,y,1) = 0, \tag{5}$$

where $\sigma_- = ah^2\nu^{-1}$ and $\sigma_+ = bh^2\nu^{-1}$ correspond to the non-dimensional strain rates of the lower and upper plates, respectively. There are two orthogonal straight lines, one in each of the boundary planes, where the velocity is zero (non-stretching lines), shown as dashed lines in Fig. 1.

In what follows, we assume the flow solution admits the solenoidal self-similar ansatz

$$u(x,y,z,t) = xf'(z,t), \; v(x,y,z,t) = yg'(z,t), \; w(x,y,z,t) = -(f+g), \tag{6}$$

where $f(z,t)$ and $g(z,t)$ are time dependent functions defined within the wall-normal domain $z \in [-1,1]$, and primes henceforth denote differentiation with respect to the nondimensional wall-normal coordinate z. After formal substitution of (6) into the incompressible Navier-Stokes equa-

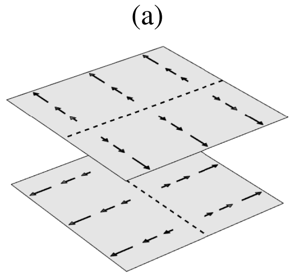

FIG. 2. Four possible shrinking-stretching configurations of the plates as a function of α. (a) $0 < \alpha < \pi/2$ (top stretches, bottom stretches), (b) $\pi/2 < \alpha < \pi$ (top shrinks, bottom stretches), (c) $\pi < \alpha < 3\pi/2$ (top shrinks, bottom shrinks), and (d) $3\pi/2 < \alpha < 2\pi$ (top stretches, bottom shrinks).

tions (3), and differentiation with respect the wall-normal variable, we obtain the nonlinearly coupled equations

$$\partial_t f'' = f^{iv} + (f+g)f''' - (f'-g')f'', \tag{7a}$$

$$\partial_t g'' = g^{iv} + (f+g)g''' + (f'-g')g''. \tag{7b}$$

Following Ayats *et al.* (2021), we assume zero mass-flux along finite vertical planes parallel to the x and y axes, so that the solutions f and g of system (7) satisfy the boundary conditions

$$f(-1) = 0, \quad f'(-1) = R\sin\alpha, \quad f(1) = 0, \quad f'(1) = 0, \tag{8a}$$

$$g(-1) = 0, \quad g'(-1) = 0, \quad g(1) = 0, \quad g'(1) = R\cos\alpha, \tag{8b}$$

where $R = \sqrt{\sigma_+^2 + \sigma_-^2}$ is the Reynolds number, and $0 \leq \alpha \leq 2\pi$ measures the relative strength of the two stretching walls (Marques *et al.*, 2017). This gives rise to four possible stretching-shrinking configurations of the plates, depicted in Fig. 2.

A Stokesian flow solution of (7), satisfying $f^{iv} = g^{iv} = 0$ and boundary conditions (8), can be easily obtained after neglecting the nonlinear terms. This solution is given by the third order polynomials

$$f_0(z) = \frac{\sigma_-}{4}(z-1)^2(z+1) = \frac{R\sin\alpha}{4}(z^3 - z^2 - z + 1), \tag{9a}$$

$$g_0(z) = \frac{\sigma_+}{4}(z+1)^2(z-1) = \frac{R\cos\alpha}{4}(z^3 + z^2 - z - 1), \tag{9b}$$

becoming a good approximation of the exact solution for small Reynolds numbers, as seen in Ayats *et al.* (2021). Henceforth in this study, we will characterize the dynamical properties of the flow by monitoring the time evolution of the three quantities

$$U(z,t) = u(1,1,z,t) = f', \quad V(z,t) = v(1,1,z,t) = g', \quad W(z,t) = w(1,1,z,t) = -(f+g), \tag{10}$$

that is, the three velocity components of the fluid at $x = y = 1$. From them, the velocity field everywhere (6) can be easily obtained: $(u,v,w)(x,y,z,t) = (xU(z,t), yV(z,t), W(z,t))$. For simplicity, these components will hereafter be denoted by $U(z)$, $V(z)$ and $W(z)$ whenever the flow field is steady, and by $U(t)$, $V(t)$ and $W(t)$ when the unsteady flow is evaluated at the midpoint wall-normal coordinate $z = 0$.

The governing equations, the flow domain and the non-stretching lines are invariant under the symmetry H consisting in a half turn (rotation of π) around the straight line $x = y = 0$, $z = 0$: $(x,y,z) \mapsto (y,x,-z)$. The action of H on the velocity field is

$$H : [u,w,w](x,y,z,t) \to [v,u,-w](y,x,-z,t). \tag{11}$$

However, the boundary conditions are not H-invariant, and in fact H exchanges σ_+ and σ_-, or what is the same change α into $\pi/2-\alpha$. A velocity field for parameter values (R,α) is transformed by H into a velocity field for different parameter values $(R,\pi/2-\alpha)$. We can explicitly write

$$H : [u,w,w](x,y,z,t;R,\alpha) \to [v,u,-w](y,x,-z,t;R,\pi/2-\alpha). \tag{12}$$

The symmetry H is only a symmetry of the governing equations plus boundary conditions for the parameter values $\alpha = \pi/4$ and $\alpha = 5\pi/4$, the case where the two boundary planes are stretching at the same rate, $\sigma_+ = \sigma_-$. The action of H on the functions f, g, U, V and W is (Ayats *et al.*, 2021)

$$H : [f,g](z,t;R,\alpha) \to [-g,-f](-z,t;R,\pi/2-\alpha). \tag{13a}$$

$$H : [U,V,W](z,t;R,\alpha) \to [V,U,-W](-z,t;R,\pi/2-\alpha). \tag{13b}$$

III. COMPUTATIONAL METHODS

In what follows, we explore time-dependent flow solutions of (7). To simplify the numerical setting, we introduce the splittings

$$f(z,t) = f_0(z) + F(z,t), \; g(z,t) = g_0(z) + G(z,t), \tag{14}$$

where $f_0(z)$ and $g_0(z)$ correspond to the basic Stokes profile (9), satisfying the boundary conditions (8), and $F(z,t)$ and $G(z,t)$ are deviations from this profile, satisfying Dirichlet-Neumann homogeneous boundary conditions

$$F(\pm 1,t) = G(\pm 1,t) = F'(\pm 1,t) = G'(\pm 1,t) = 0. \tag{15}$$

After introducing (14) in (7), the initial-boundary value problem reads

$$\begin{aligned} \partial_t F'' &= F^{iv} + (f_0 + F + g_0 + G)(f_0''' + F''') - (f_0' + F' - g_0' - G')(f_0'' + F'') \\ \partial_t G'' &= G^{iv} + (f_0 + F + g_0 + G)(g_0''' + G''') + (f_0' + F' - g_0' - G')(g_0'' + G''). \end{aligned} \tag{16}$$

or simply

$$\begin{aligned} \partial_t F'' &= L(F) + N_1(F, G, f_0, g_0) \\ \partial_t G'' &= L(G) + N_2(F, G, f_0, g_0), \end{aligned} \tag{17}$$

where L stands for the fourth order linear biharmonic operator, and N_1 and N_2 for nonlinear differential operators, implicitly depending on the two parameters R and α through the Stokesian profiles f_0 and g_0. Equilibrium solutions (F_0, G_0) of (17) satisfying $(\partial_t F_0'', \partial_t G_0'') = (0,0)$ were computed by Ayats *et al.* (2021) using a Legendre spectral method. Accordingly, we discretize (17) using the same type of spectral expansions for the time-dependent deviation fields $F(z,t)$ and $G(z,t)$, of the form

$$\begin{bmatrix} F(z,t) \\ G(z,t) \end{bmatrix} = \sum_{m=0}^{M} a_m(t)\Phi_m^{(1)}(z) + b_m(t)\Phi_m^{(2)}(z), \tag{18}$$

where

$$\Phi_m^{(1)}(z) = \begin{bmatrix} \phi_m(z) \\ 0 \end{bmatrix}, \ \Phi_m^{(2)}(z) = \begin{bmatrix} 0 \\ \phi_m(z) \end{bmatrix}, \ \phi_m(z) = (1 - z^2)^2 P_m(z), \tag{19}$$

and where $P_m(z)$ is the mth Legendre polynomial. We introduce the inner Hermitian product between two arbitrary vector fields $\Psi(z) = [\psi_1(z)\ \psi_2(z)]^{\mathrm{T}}$ and $\Theta(z) = [\theta_1(z)\ \theta_2(z)]^{\mathrm{T}}$

$$(\Psi, \Phi) \doteq \int_{-1}^{1} \Psi(z)^{\mathrm{T}} \cdot \Theta(z)\, \mathrm{d}z. \tag{20}$$

The system of nonlinear partial differential equations (17) is transformed to a system of ordinary differential equations for the spectral coefficients $\mathbf{a}(t) = [a_0\, a_1\, \cdots a_M]^{\mathrm{T}}$ and $\mathbf{b}(t) = [b_0\, b_1\, \cdots b_M]^{\mathrm{T}}$ by a Galerkin projection method. This transformation involves a formal substitution of the spectral expansion (18) in (17), followed by the Hermitian projection on the set of orthogonal vector fields

$\Phi_m^{(1)}$ and $\Phi_m^{(2)}$ defined in (19), leading to the $2(M+1)$-dimensional dynamical system for the amplitude coefficients $\mathbf{a}$ and $\mathbf{b}$:

$$\sum_{m=0}^{M} A_{\ell m}\frac{\mathrm{d}a_m}{\mathrm{d}t} = \sum_{m=0}^{M} B_{\ell m}\, a_m + N_{\ell,1}(\mathbf{a},\mathbf{b}) \tag{21a}$$

$$\sum_{m=0}^{M} A_{\ell m}\frac{\mathrm{d}b_m}{\mathrm{d}t} = \sum_{m=0}^{M} B_{\ell m}\, b_m + N_{\ell,2}(\mathbf{a},\mathbf{b}) \tag{21b}$$

where the matrix elements $A_{\ell m}$ and $B_{\ell m}$ are given by Legendre inner products

$$A_{\ell m} = \int_{-1}^{1} \phi_\ell\, \phi_m^{''}\,\mathrm{d}z, \qquad B_{\ell m} = \int_{-1}^{1} \phi_\ell\, \phi_m^{iv}\,\mathrm{d}z. \tag{22}$$

Similarly, $N_{\ell,1}(\mathbf{a},\mathbf{b})$ and $N_{\ell,2}(\mathbf{a},\mathbf{b})$ are the projections of the nonlinear terms

$$N_{\ell,1} = \int_{-1}^{1} \phi_\ell N_1(\mathbf{a},\mathbf{b})\,\mathrm{d}z, \qquad N_{\ell,2} = \int_{-1}^{1} \phi_\ell N_2(\mathbf{a},\mathbf{b})\,\mathrm{d}z. \tag{23}$$

The wall-normal integrals appearing above are accurately computed using Gauss-Legendre quadrature formulas (Quarteroni, Sacco, and Saleri, 2010). For simplicity, we henceforth express the resulting system of nonlinear ordinary differential equations (21) as

$$\mathbb{A}\dot{\mathbf{x}} = \mathbb{B}\mathbf{x} + \mathbb{N}(\mathbf{x}), \tag{24}$$

where $\mathbf{x} = [a_0\; a_1\; \cdots a_M\; b_0\; b_1\; \cdots b_M]^{\mathrm{T}}$, and $\dot{\mathbf{x}}$ stands for time differentiation.

The time integration is carried out using a 4th-order IMEX method (BDF4 backward-differences linearly-implicit method for the linear biharmonic term and 4th-order explicit extrapolation of the nonlinear term) with the linear multistep formula

$$\begin{aligned}(25\mathbb{A} - 12\Delta t\mathbb{B})\mathbf{x}^{(j+1)} = \\ \mathbb{A}(48\mathbf{x}^{(j)} - 36\mathbf{x}^{(j-1)} + 16\mathbf{x}^{(j-2)} - 3\mathbf{x}^{(j-3)}) \\ + \Delta t(48\mathbb{N}^{(j)} - 72\mathbb{N}^{(j-1)} + 48\mathbb{N}^{(j-2)} - 12\mathbb{N}^{(j-3)}),\end{aligned} \tag{25}$$

where $\mathbf{x}^{(j)} = \mathbf{x}(j\Delta t)$, and where the time-stepper is initialized using a 4th-order Runge-Kutta method (Meseguer, 2020). In all computations presented here, the time step used ranges within the interval $\Delta t \in [1\times 10^{-4}, 2.5\times 10^{-4}]$. Decreasing the time step below those values did not result in noticeable changes of the computed time-dependent solutions. As to the spatial Legendre discretization, the number of Legendre modes lied within the interval $M \in [35, 50]$, following the resolutions previously used by Ayats *et al.* (2021).

A. Linear stability of steady flows

Let $(F_0(z), G_0(z))$ be an equilibrium solution of system (16), satisfying $\partial_t F_0'' = \partial_t G_0'' = 0$. For the linear stability analysis of this steady profile, we perturb the flow by adding infinitesimal perturbations of order $O(\varepsilon)$, so that the disturbed profile reads

$$\begin{aligned} F(z,t) &= F_0(z) + \varepsilon \widetilde{F}(z,t), \\ G(z,t) &= G_0(z) + \varepsilon \widetilde{G}(z,t), \end{aligned} \tag{26}$$

where $\widetilde{F}(z,t) = \mathrm{e}^{\lambda t}\mathscr{F}(z)$ and $\widetilde{G}(z,t) = \mathrm{e}^{\lambda t}\mathscr{G}(z)$, with $\mathscr{F}(z)$ and $\mathscr{G}(z)$ being the eigenfunctions of the perturbation associated with the eigenvalue λ, satisfying homogeneous boundary conditions

$$\mathscr{F}(\pm 1) = \mathscr{G}(\pm 1) = \mathscr{F}'(\pm 1) = \mathscr{G}'(\pm 1) = 0. \tag{27}$$

Introducing the perturbed fields (26) in (16) and neglecting $O(\varepsilon^2)$ terms, leads to the system of linear partial differential equations

$$\begin{aligned} \lambda \mathscr{F}'' = {} & \mathscr{F}^{iv} + (f_0 + F_0 + g_0 + G_0)\mathscr{F}''' + (f_0''' + F_0''')(\mathscr{F} + \mathscr{G}) \\ & - (f_0'' + F_0'')(\mathscr{F}' - \mathscr{G}') - (f_0' + F_0' - g_0' - G_0')\mathscr{F}'', \\ \lambda \mathscr{G}'' = {} & \mathscr{G}^{iv} + (f_0 + F_0 + g_0 + G_0)\mathscr{G}''' + (g_0''' + G_0''')(\mathscr{F} + \mathscr{G}) \\ & + (g_0'' + G_0'')(\mathscr{F}' - \mathscr{G}') + (f_0' + F_0' - g_0' - G_0')\mathscr{G}'', \end{aligned} \tag{28}$$

or, for simplicity,

$$\begin{aligned} \lambda \mathscr{F}'' &= C_1(\mathscr{F}, \mathscr{G}, F_0, G_0, f_0, g_0), \\ \lambda \mathscr{G}'' &= C_2(\mathscr{F}, \mathscr{G}, F_0, G_0, f_0, g_0), \end{aligned} \tag{29}$$

where C_1 and C_2 are the linear actions resulting from the biharmonic operator and advective terms, linearized in a neighborhood of (F_0, G_0). We again discretize the eigenperturbations using Legendre spectral expansions

$$\begin{bmatrix} \mathscr{F}(z) \\ \mathscr{G}(z) \end{bmatrix} = \sum_{m=0}^{M} \widetilde{a}_m \Phi_m^{(1)}(z) + \widetilde{b}_m \Phi_m^{(2)}(z), \tag{30}$$

so that, after the Hermitian projection, the linear stability analysis is reduced to solve a $2(M+1)$-dimensional generalized eigenvalue problem of the form

$$\lambda \mathbb{A}\mathbf{x} = \mathbb{C}\mathbf{x}. \tag{31}$$

In the present work, the linear stability of all the equilibria formerly reported in Ayats *et al.* (2021) has been monitored by computing the ten rightmost eigenvalues of (31) using Arnoldi iteration combined with suitable Cayley transformations in the complex plane (Trefethen and Bau, 1997).

B. Computation and Floquet linear stability of time-periodic flows

To compute relative periodic orbits beyond their region of linear stability, a Poincaré-Newton-Krylov (PNK) method is devised. The method is essentially an adaptation of the one used for the computation of modulated traveling waves in plane Poiseuille flow (Mellibovsky and Meseguer, 2015; Ayats, Meseguer, and Mellibovsky, 2020). In this case, the method solves the nonlinear system of equations resulting from root finding for the map defined by consecutive crossings of a Poincaré section $\mathbb{P}$:

$$\mathbf{x} \to \widetilde{\mathbf{x}} = \mathbb{P}(\mathbf{x}) = \varphi(\mathbf{x}; t(\mathbf{x})), \tag{32}$$

where $\varphi(\cdot;t)$ is the action of the uniparametric group or flow generated by (24), and $t(\mathbf{x})$ is the flight-time of the return map associated with $\mathbf{x}$. Due to the large dimension of the dynamical system, periodic orbits are obtained by solving $\mathbb{P}(\mathbf{x}) - \mathbf{x} = 0$ by means of a Jacobian-free Newton-Krylov method (Kelley, 2003; Knoll and Keyes, 2004). In the present analysis, all the reported periodic orbits have been converged satisfying the tolerance criterion $||\mathbb{P}(\mathbf{x}) - \mathbf{x}|| < 10^{-10}$. Once a periodic orbit $\mathbf{x}_0$ has been converged to the required tolerance, its linear stability analysis consists in computing the leading (largest moduli) eigenvalues of the linearized Poincaré map in a neighborhood of $\mathbf{x}_0$. The aforementioned leading eigenvalues are accurately approximated by means of the Arnoldi iteration (Trefethen and Bau, 1997) applied on the linearized action of the Jacobian of the Poincaré map at $\mathbf{x}_0$,

$$\mathrm{D}_{\varepsilon}\mathbb{P}(\mathbf{x}_0) \approx \frac{\mathbb{P}(\mathbf{x}_0 + \varepsilon) - \mathbb{P}(\mathbf{x}_0)}{||\varepsilon||}, \tag{33}$$

where ε is a small numerical perturbation from the periodic orbit. In this case, the norm of the perturbation ε must be suitably chosen, so that it genuinely captures the linearized dynamics in a neighborhood of $\mathbf{x}_0$, whilst $\varphi(\mathbf{x}_0 + \varepsilon; t)$ is accurately computed by the RK4-IMEX4 scheme before described. In this work, the computed leading eigenvalues are provided with a relative error smaller than 0.1%.

IV. OSCILLATORY INSTABILITIES OF STEADY FLOWS

In Ayats *et al.* (2021), up to five non-symmetrically related families of steady flows were identified, and tracked within the parameter space (α, R). When increasing the Reynolds number, these families of steady solutions interact by means of saddle-node and codimension-2 cusp bifurcations leading to intricated branches, especially in the neighborhood of $\alpha = 5\pi/4$, when both membranes

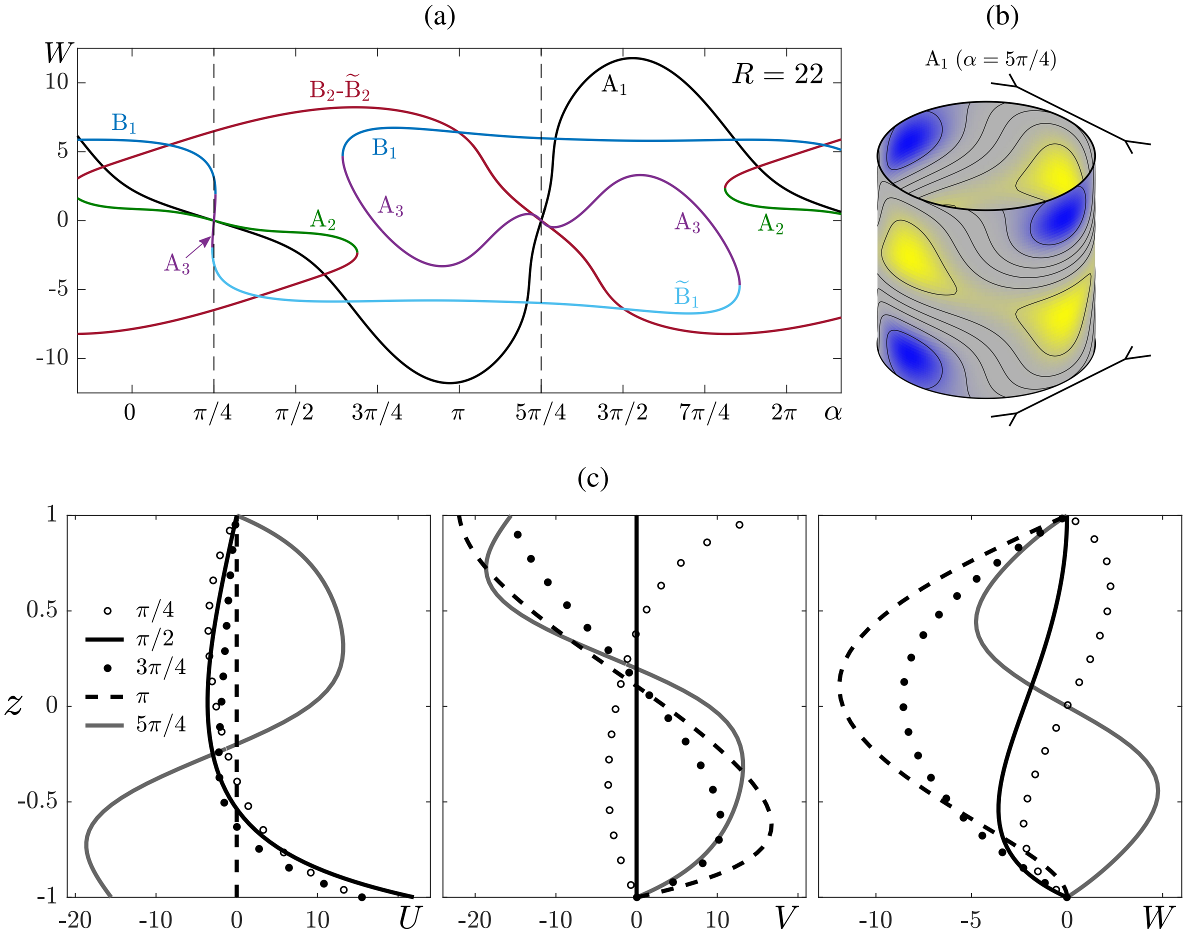

FIG. 3. Families of steady flows formerly identified in Ayats *et al.* (2021) for $R = 22$. (a) Wall-normal velocity of the steady flows as defined in (10) at $z = 0$, covering all possible stretching-shrinking acceleration rates as a function of α. Colored branches are linearly unstable. The branch A_1 (solid black) is linearly stable. (b) Radial velocity field of stable A_1 steady solution for identical shrinking deceleration rates of the plates ($\alpha = 5\pi/4$). (c) $U(z)$, $V(z)$ and $W(z)$ steady velocity profiles of A_1 solution as a function of the wall-normal coordinate z, and for selected stretching-shrinking acceleration rates.

are shrinking at the same deceleration rate. Figure 3a shows the wall-normal velocity of the aforementioned five steady flow families for $R = 22$, covering all possible stretching-shrinking acceleration rates, parametrized by α. Following Ayats *et al.* (2021), these families are designated by A_1, A_2, A_3, B_1, and B_2. The two remaining families $\widetilde{\mathrm{B}}_1$ and $\widetilde{\mathrm{B}}_2$ are symmetrically related to B_1, B_2, respectively, by the H symmetry: $\widetilde{\mathrm{B}}_1 = H\,\mathrm{B}_1$, and $\widetilde{\mathrm{B}}_2 = H\,\mathrm{B}_2$.

To uncover the dynamical relevance of these steady flows, the linear Arnoldi stability analysis formulated in §III A has been comprehensively applied to the aforementioned solutions within the parameter range $(\alpha, R) \in [0, 2\pi] \times [0, 33]$. This analysis concludes that the A_1 branch is the only linearly stable flow for low or moderate Reynolds numbers. The remaining families of steady solutions have been found to be unstable, even for the lowest Reynolds numbers they were identified in Ayats *et al.* (2021). Despite some of these unstable branches have been found to undergo several bifurcations leading to other steady or time-dependent flows, the latter appear to be dynamically irrelevant, as they inherit the instability of the steady branches they stem from. For this reason, we henceforth restrict ourselves to report only those instabilities corresponding to the stable branch A_1.

Figure 3b shows the radial velocity distribution of the A_1 stable steady flow, for $R = 22$ and $\alpha = 5\pi/4$. This solution originates from the Stokesian flow (9) and, when both plates are shrinking at the same deceleration rate, it is characterized by two staggered near-wall layers of inflow (blue) and outflow (yellow) orthogonal jets. The three steady velocity profiles $U(z)$, $V(z)$, and $W(z)$, as defined in (10), are depicted in Fig. 3c for five different values of α, covering distinguished stretching-shrinking acceleration rates of the top and bottom plates. The motivation for illustrating the solution A_1 for $\alpha = 5\pi/4$ in Fig. 3b is that the oscillatory flows identified in this study arise precisely when both plates are shrinking at identical or similar deceleration rates.

The routes that lead to oscillatory and other unsteady non-periodic flows are far from being trivial. Figure 4 outlines the main results of the present study, as they will be later on described in detail in the current and forthcoming sections. This diagram is a zoom-in of Figures 9a and 9c formerly reported in Ayats *et al.* (2021), covering the range $(\alpha, R) \in [3.6, 4.25] \times [23.0, 32.0]$, where the stable steady solution A_1 has been found to exhibit oscillatory instabilities. To better illustrate the mechanisms that lead to oscillatory flows, panels (a), (b), and (c) of Fig. 5 depict the α-continuation of the solution branches A_1 and A_3 for $R = 23$, $R = 26$ and $R = 26.7$, respectively. For $R < 23.4$, the A_1 branch (solid black curve) is univalued and linearly stable, whereas A_3 (solid gray curve) is unstable. However, for $R = 23$ (depicted in Fig. 5a), the A_1 branch already exhibits two inflectional points, anticipating a simultaneous pair of cuspidal bifurcations, that appear at a critical Reynolds number $R = 23.4$ (red bullets C_3 and C_4 in Fig. 4), as previously reported in Ayats *et al.* (2021). For $R > 23.4$, the A_1 branch develops a pair of saddle-node bifurcation points emerging from C_3 and C_4 (black solid curves in Fig. 4). These saddle-node points are illustrated in Figs. 4 and 5b for $R = 26$ (squares SN_1, SN_1', SN_2 and SN_2'). Within the range $23.4 < R < 25.5$, the family of A_1 steady solutions bounded between the two outer saddle-node boundaries is linearly stable. However, for $R = 25.5$ and $\alpha = 5\pi/4$, this branch exhibits a Hopf bifurcation (white bullet

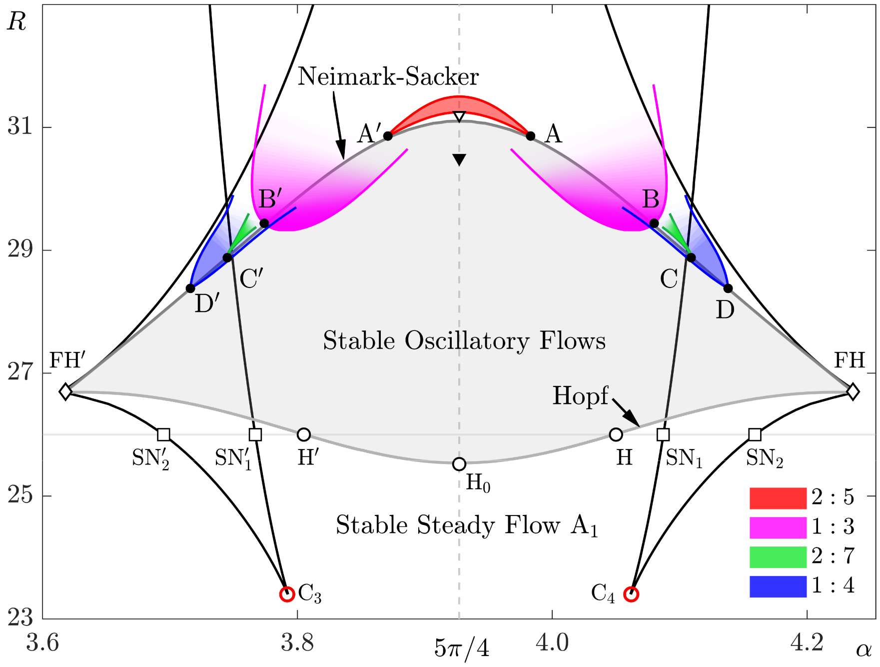

FIG. 4. Bifurcation scenarios leading to time-periodic, quasiperiodic, phase-locked, and chaotic flows. Stable periodic flows exist within the light gray shaded region, bounded by the Hopf and Neimark-Sacker bifurcation boundaries (gray solid curves). Resonance locking regions (Arnold tongues) 2 : 5 (red), 1 : 3 (magenta), 2 : 7 (green) and 1 : 4 (blue).

H_0 along the symmetry line $\alpha = 5\pi/4$ of Fig. 4). As the Reynolds number is increased, this Hopf bifurcation progressively expands outwards from the $\alpha = 5\pi/4$ symmetry line, destabilizing the central segment of the A_1 branch (gray solid segment of curve between points H and H′ in Fig. 5b for $R = 26$). Continuation of the loci of the two symmetrical Hopf bifurcation points leads to the Hopf instability boundary, depicted as a solid light gray curve in Fig. 4, spreading outwards the symmetry line $\alpha = 5\pi/4$. The growth of the Hopf boundary is however hampered immediately after by the merging of the A_1 and A_3 branches through a pinch mechanism, engendering an isola of solutions (gray solid curve in Fig. 5c for $R = 26.7$) whose central portion now inherits the Hopf instability. As a result of this merging, the Hopf instability eventually reaches the bounding saddle-nodes of the A_1-A_3 isola, resulting in a Fold-Hopf codimension-2 bifurcation point (diamonds FH and FH′ in Fig. 4). The merging of branches A_1 and A_3 does not affect the topological structure of the flow; see solution point E located at the isola in Fig. 5c, whose velocity distribution is depicted in Fig. 5d, still showing the two staggered inflow-outflow orthogonal near-wall jets. However, the steady flows along the dislocated branch are different, as it can be seen from the solution D in

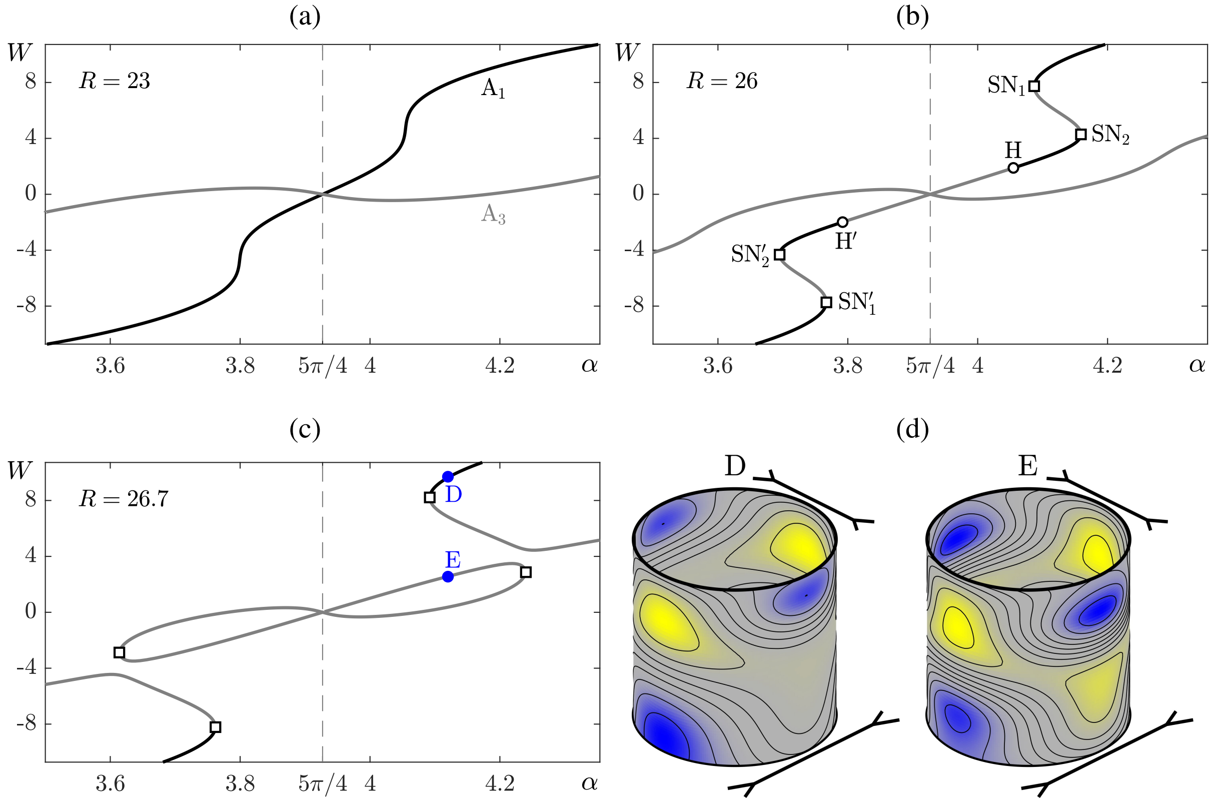

FIG. 5. Hopf bifurcation route leading to oscillatory flows. (a), (b) and (c) show wall-normal velocity W at mid plane coordinate $(x,y,z) = (1,1,0)$ of the A$_1$ and A$_3$ steady flows solutions for $R = 23$, $R = 26$ and $R = 26.7$, respectively. Solid black (gray) curves stand for stable (unstable) solutions. (d) Cylindrical cross-section of radial velocity v_r isocontours of detached steady flow solutions D (stable) and E (Hopf unstable) indicated in (c) for $R = 26.7$.

Fig. 5c, whose velocity distribution has lost one of the near-wall jets close to the bottom plate (Fig. 5d).

The Hopf bifurcation that takes place along the A$_1$ − A$_3$ isola branch leads to stable oscillatory flows (i.e., stable limit cycles), whose main features are shown in Fig. 6 for $\alpha = 5\pi/4$, where panel (a) depicts time-series of the three velocity components of the flow defined in (10), and panel (b) shows U-W phase portrait projections of three stable periodic orbits for $R = 26$, $R = 28$ and $R = 30.5$. For this particular value of α, the domain along with the governing equations are invariant under the H-symmetry transformation (12). According to equivariant bifurcation theory, the resulting time-periodic solution arising from the Hopf instability of the H-symmetric steady flow A$_1$ may only break that symmetry by means of the so-called *half-period shift and flip*

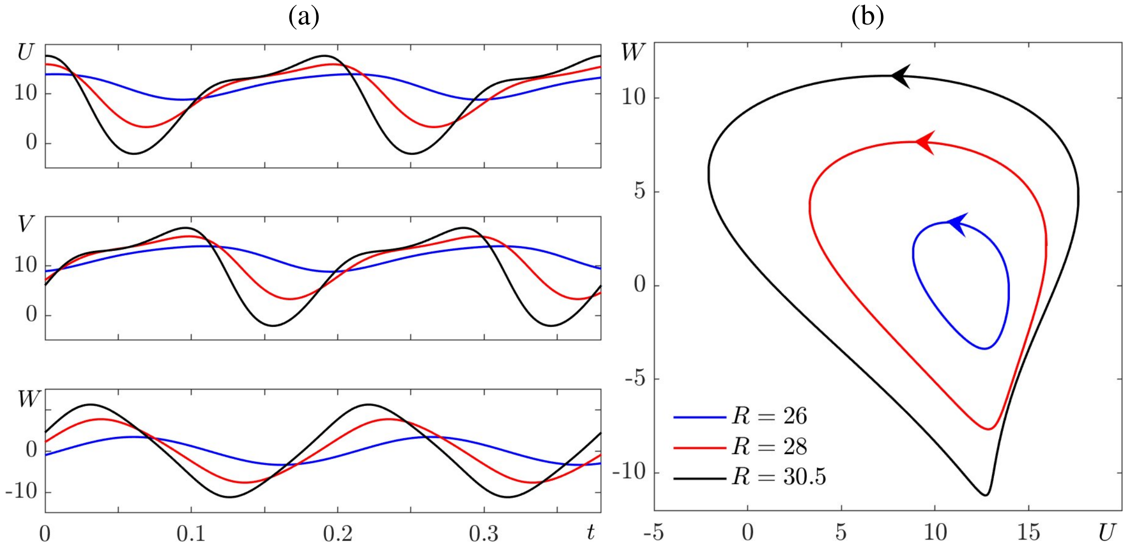

FIG. 6. Time dependence characterization of oscillatory flows arising from the Hopf bifurcation of the A_1 steady flow for $\alpha = 5\pi/4$, and $R = 26$, $R = 28$, and $R = 30.5$. Color coding in (a) as indicated in (b); see legends. (a) Time-series of the oscillatory flow velocity components $U(t)$, $V(t)$, and $W(t)$, as defined in (10). (b) (U,W)-phase portrait projection of the bifurcated periodic orbits.

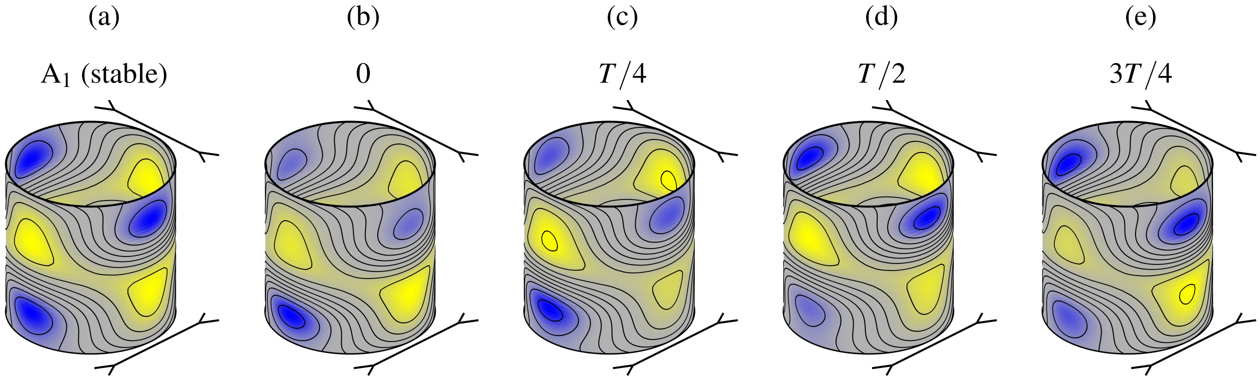

FIG. 7. Isocontours of radial velocity for $\alpha = 5\pi/4$. (a) Linearly stable steady flow A_1 for $R = 25$. (b)-(e) Snapshots of the bifurcated time-periodic flow for $R = 26$ at $t = 0$, $t = T/4$, $t = T/2$ and $t = 3T/4$. Panels (d) and (e) are related to panels (b) and (c) through the half period and flip symmetry (34), respectively.

mechanism (Kuznetsov, 2004). This symmetry breaking can be observed by simple eye inspection of the time-series of the three velocity components shown in Fig. 6a, being more apparent for $R = 30.5$, satisfying

$$(U,V,W)(t+\frac{T}{2}) = (V,U,-W)(t), \tag{34}$$

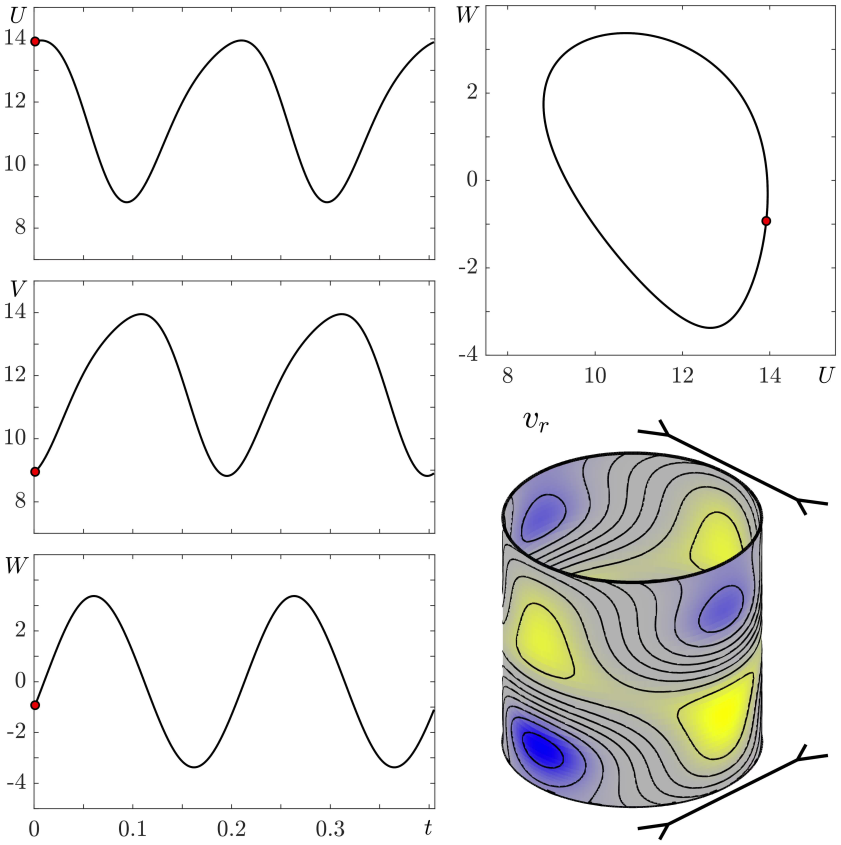

FIG. 8. Oscillatory flow for $R = 26$ and $\alpha = 5\pi/4$. First column shows the time evolution of the velocity components. Second column shows the (U,W)-phase portrait and isocontours of radial velocity v_r. Movie 1 (Multimedia view) animates the oscillatory flow during two periods (red dots in the figure correspond to the instants of time at which the isocontour frames is taken).

with T being the period of the oscillatory flow. This symmetry can also be discerned after comparing panels (b) and (c) with (d) and (e) of Fig. 7, respectively, showing snapshots of isocontours of radial velocity along a complete cycle of the stable oscillatory flow. Before the Hopf bifurcation, the steady flow A_1 is characterized by two layers of orthogonal jets of opposed orientation, aligned with the x and y directions of the top and bottom shrinking boundaries. This is illustrated in Fig. 7a, showing the inward (blue) and outward (yellow) radial velocity distribution throughout a cylindrical unit cross section. After the Hopf bifurcation, the intensity of these jets becomes modulated in time, showing an alternate predominance of the inward and outward radial velocity every half a period of the cycle. Movie 1 (Multimedia view) animates the solution along two time periods; Fig. 8 shows the snapshot of the movie at $t = 0$.

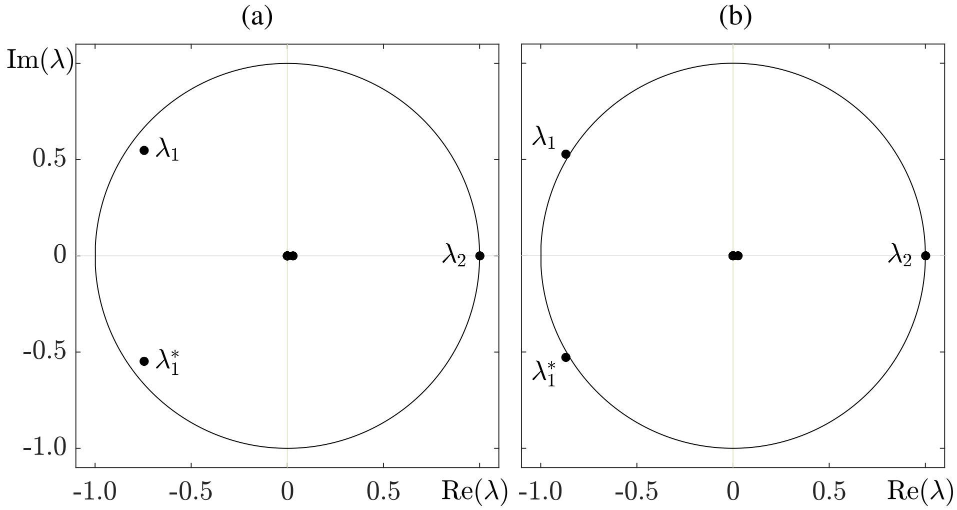

FIG. 9. Leading eigenvalues (largest modulus) of the Poincaré map of time-periodic flows for $\alpha = 5\pi/4$. (a) and (b) showing spectra of a linearly stable and linearly unstable periodic orbit for $R = 30.5$ and $R = 31.2$, denoted by black and white triangles in Fig. 4, respectively.

V. QUASIPERIODIC AND CHAOTIC FLOWS

The time-periodic flows described in section §IV have also been tracked, and their linear stability monitored. These flows are stable and take over the dynamics within a wide region of the parameters explored; gray shaded area shown in Fig. 4. However, these time-periodic flows eventually become linearly unstable for higher Reynolds numbers through a Neimark-Sacker bifurcation, typically leading to quasiperiodic flows or tori (Kuznetsov, 2004). This secondary bifurcation takes place along the Neimark-Sacker boundary depicted as a solid dark gray curve in Fig. 4. For an accurate computation of this bifurcation boundary, the leading eigenvalues (those with largest modulus) of the time-periodic flows have been computed by means of the Arnoldi method described in §III B. Figure 9 depicts the modulus-leading eigenvalues of the Poincaré map associated with the time-periodic flow for $\alpha = 5\pi/4$, slightly below and above the Neimark-Sacker bifurcation boundary. For $R = 30.5$ (black triangle in Fig. 4), the periodic orbit is still linearly stable, as its leading eigenvalues λ_1 and λ_1^* shown in Fig. 9a lie within the unit disk in the complex plane; apart from the neutral eigenvalue $\lambda_2 \approx 1$, associated with the eigenvector pointing in the direction tangent to the uniparametric group $\varphi(\cdot;t)$ induced by (24). For $R = 31.2$ (white triangle in Fig. 4), Fig. 9b clearly shows that the leading complex conjugated pair λ_1 and λ_1^* has just crossed the $|\lambda| = 1$ unit circle, with non-zero imaginary part, thus revealing a Neimark-Sacker bifurca-

M	$\|\|\varepsilon\|\|$	λ_1 (λ_1^*)	$\|\|\lambda_1\|\|$	λ_2
35	10^{-2}	$-0.8712 \pm 0.5205\,\mathrm{i}$	1.0148	1.0015
	10^{-3}	$-0.8691 \pm 0.5278\,\mathrm{i}$	1.0169	1.0015
	10^{-4}	$-0.8689 \pm 0.5286\,\mathrm{i}$	1.0171	1.0015
50	10^{-2}	$-0.8692 \pm 0.5365\,\mathrm{i}$	1.0215	1.0015
	10^{-3}	$-0.8689 \pm 0.5294\,\mathrm{i}$	1.0175	1.0015
	10^{-4}	$-0.8689 \pm 0.5287\,\mathrm{i}$	1.0171	1.0015

TABLE I. Accuracy of leading eigenvalues of the Poincaré map of the unstable periodic orbit for $\alpha = 5\pi/4$ and $R = 31.2$ (white triangle in Fig. 4) as a function of wall-normal Legendre modes M and finite-difference $||\varepsilon||$ used to approximate the action of the Jacobian.

tion. The shown spectra of eigenvalues have been computed using $M = 35$ Legendre wall-normal modes, and taking $||\varepsilon|| = 10^{-3}$ for the approximation of the linearized action of the Jacobian. Henceforth in our analysis, M and $||\varepsilon||$ are fixed to the aforementioned values, as further increase in the number of wall-normal modes, or decrease in the size of $||\varepsilon||$, did not result in significant changes in the real or imaginary parts of the eigenvalues. This is reflected in Table I, that outlines the numerical accuracy of the computed spectrum for $\alpha = 5\pi/4$, $R = 31.2$, and as a function of the number of wall-normal modes, as well as the finite-difference parameter $||\varepsilon||$.

Above the Neimark-Sacker boundary curve, the dynamics is governed by stable quasiperiodic flows (tori), usually characterized by two rationally independent frequencies (Kuznetsov, 2004). Figure 10 shows the $(U(t), W(t))$-phase portrait, Poincaré cross section, the power spectrum of the bifurcated torus, and its originating unstable periodic orbit, for $\alpha = 5\pi/4$ and $R = 31.2$ (white triangle in Fig. 4), just above Neimark-Sacker bifurcation boundary. This unstable periodic orbit is characterized by a single frequency $f_1 \approx 5.32$ (see power spectrum in Fig. 10c ; in red). The bifurcated torus inherits this main frequency, but it also incorporates a secondary one $f_2 \approx 2.21$, as it can be clearly identified in the Fourier's power spectrum shown in Fig. 10c (black). This secondary frequency integrates a modulation in the time-periodicity of the formerly stable oscillatory flow, as illustrated in the phase portrait of the torus T_2 shown in Fig. 10a (gray curve). To better discern the modulation introduced by the quasiperiodic behavior, the originating unstable periodic orbit (UPO) has also been included in Fig. 10a (red curve), along with a fragment of the stable quasiperiodic orbit (black). Three points along the quasiperiodic orbit have been selected in

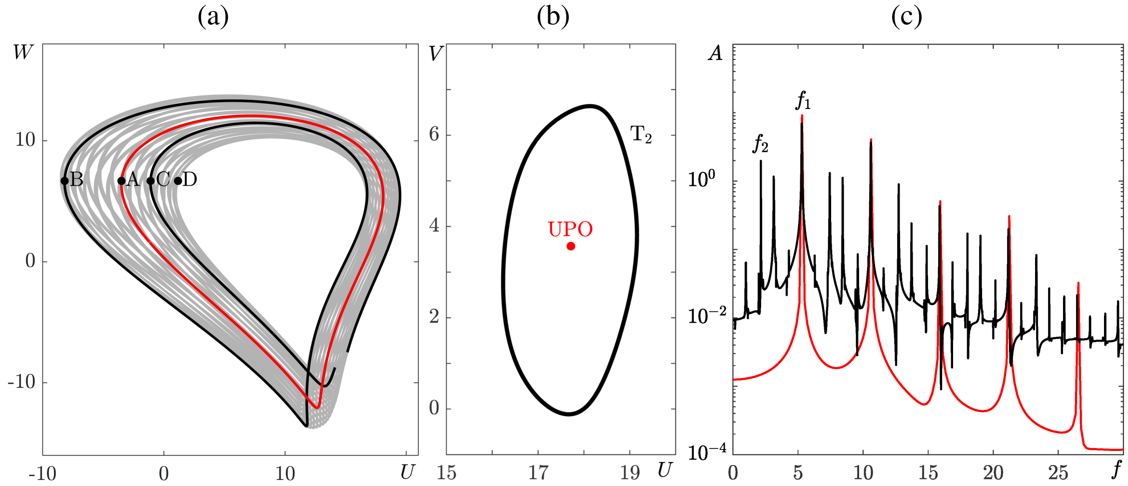

FIG. 10. Dynamics of a quasiperiodic flows for $(\alpha, R) = (5\pi/4, 31.2)$, immediately after the Neimark-Sacker bifurcation. (a) $(U(t), W(t))$-phase portrait of unstable periodic orbit (red) and the stable torus T$_2$ (gray). The black curve shows part of the quasiperiodic orbit. (b) Poincaré section $W = 3$ of the unstable periodic orbit (UPO; red disk) and torus (black curve) shown in (a). (c) Fourier power spectra corresponding to the unstable periodic orbit (red) and torus (black), indicating the UPO's frequency f_1, and the new frequency f_2, leading to a quasiperiodic regime.

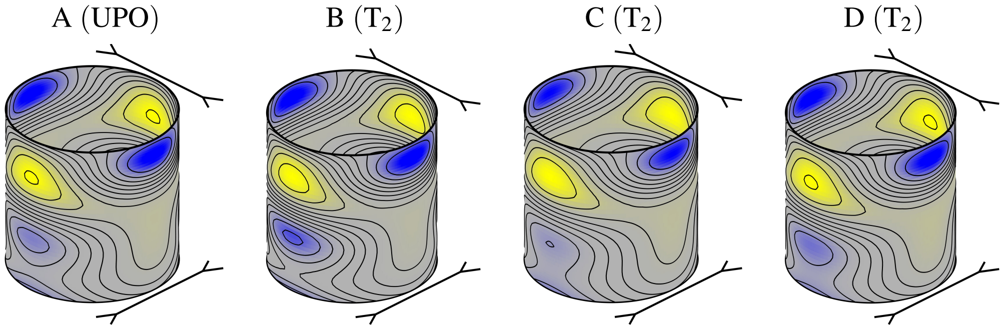

FIG. 11. Isocontours of radial velocity corresponding to local $U(t)$-minima points A (UPO), and B,C, and D (T$_2$ orbit), indicated in Fig. 10a.

Fig. 10a, at instants of time where the U component of the velocity field reaches a local minimum (black disks B, C and D), along with a reference point A of the UPO. The flow fields corresponding to points A, B, C and D are depicted in Fig. 11, where the time modulation introduced by the new frequency can be clearly recognized for example by looking at the pulsating intensity of the inflow jets (blue), in the lower part of the cross-sectional projection of radial velocity of the panels

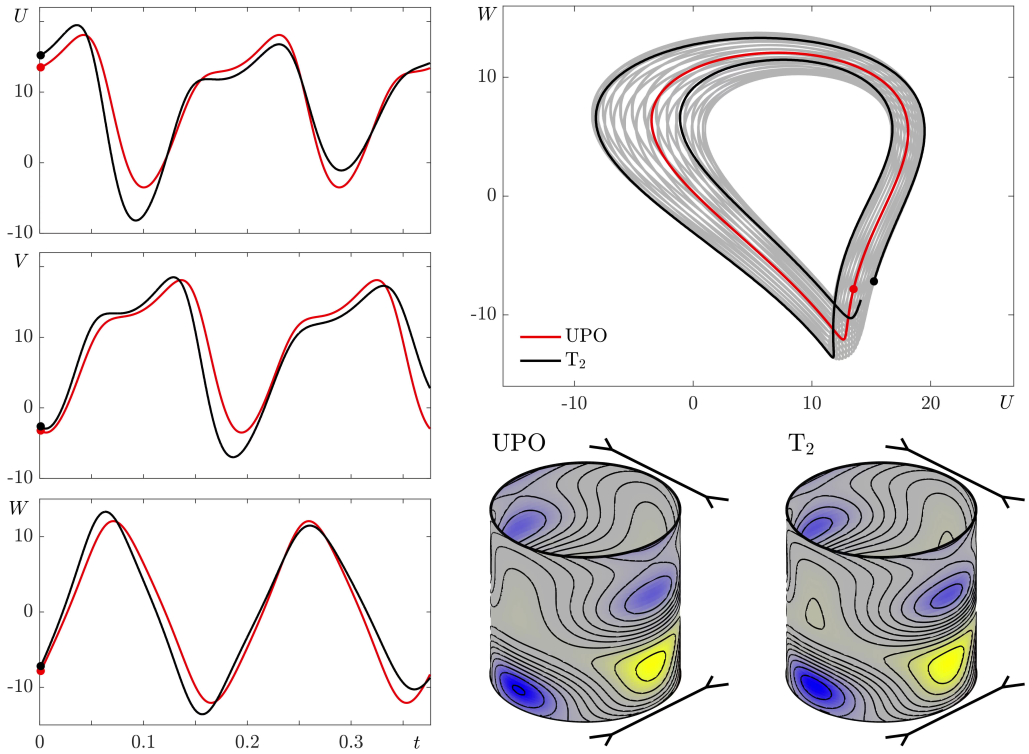

FIG. 12. Quasiperiodic flow for $R = 31.2$ and $\alpha = 5\pi/4$. First column shows the time evolution of the velocity components. Second column shows the (U,W)-phase portrait and isocontours of radial velocity v_r. Movie 2 (Multimedia view) animates the quasiperiodic flow during two periods of f_1 (red and black dots in the figure correspond to the instants of time at which the isocontour frames are taken).

B, C and D. The movie 2 (Multimedia view) animates T$_2$ and the UPO along the black curve in Fig. 10a; Fig. 12 shows the snapshot of the movie at $t = 0$.

In general, quasiperiodic flows may also exhibit tertiary instabilities when increasing the Reynolds number, often leading to more complicated or even chaotic dynamics. Within the context of self-similar flows, former studies have reported transition to chaotic attractors by means of period-doubling cascades (Watson *et al.*, 1990; Espín and Papageorgiou, 2009; Marques *et al.*, 2017). In the present study, chaotic flows seem to emerge through the classical Ruelle-Takens-Newhouse scenario (Newhouse, Ruelle, and Takens, 1978), where the stable T$_2$ tori, formerly produced at the Neimark-Sacker bifurcation, eventually lose their differentiability by means of a *homoclinic Poincaré tangle*, commonly producing a strange attractor before a third rationally independent frequency may arise (Abraham and Shaw, 1992). Figure 13 shows a zoom-in of the

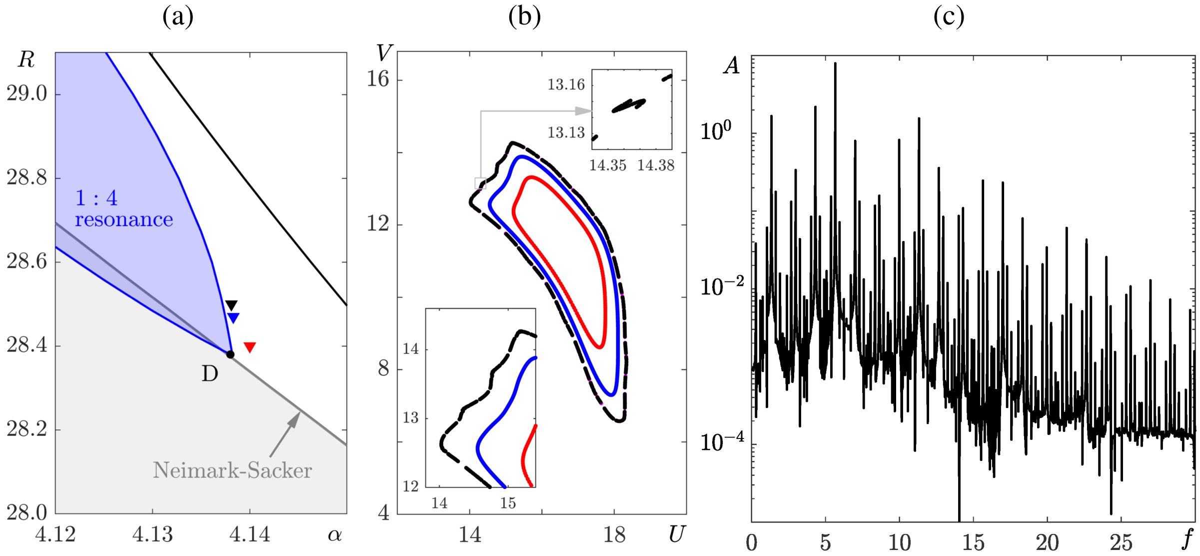

FIG. 13. Ruelle-Takens-Newhouse transition scenario to chaotic flows. (a) Parameter region where strange attractors have been identified. (b) (U,V) projection of Poincaré cross section at $W = 3$ of stable tori (red and blue) and chaotic attractor (black) at the points indicated in (a) with triangles using the same color code. (c) Power spectrum of $U(t)$ for the chaotic regime.

region where chaotic flows have been identified, far away from the symmetry line $\alpha = 5\pi/4$. Within this region, a stable torus T_2 at $(\alpha, R) = (4.14, 28.4)$, red triangle in Fig. 13a, has just emerged from the Neimark-Sacker bifurcation (red Poincaré section in Fig. 13b). This torus can be tracked within this region by following a suitable path, consisting in gradually increasing the Reynolds number whilst reducing α. At $(\alpha, R) = (4.1378, 28.5)$, blue triangle in Fig. 13a, the torus has increased in amplitude (blue cross section in Fig. 13b). At $(\alpha, R) = (4.1371, 28.55)$, the torus differentiability has already been lost (black triangle in Fig. 13a and corresponding cross-section in Fig. 13b), and a strange attractor has already been formed. In particular, Fig. 13b clearly shows a wrinkled topology of the strange attractor, still reminiscent of the Poincaré homoclinic tangle. The power spectrum of the time-series of $U(t)$, depicted in Fig. 13c, shows that the dynamics is weakly chaotic. We anticipate here that further increase in the Reynolds number, or slight variations in α typically destroy this attractor, relaminarizing to other stable periodic states. As a matter of fact, chaotic flows in the current problem seem to be quite elusive and non-generic, as the quasiperiodic dynamics above the Neimark-Sacker bifurcation curve seem to consistently collapse with resonant periodic regions, a phenomenon that will be addressed in section §VI.

points	A	A′	B	B′	C	C′	D	D′
α	3.983	3.871	4.237	4.082	4.109	3.745	4.138	3.716
R	30.86	30.86	29.44	29.44	28.90	28.90	28.38	28.38

TABLE II. Coordinates of the points where the resonance regions, shown in Fig. 4, are born.

VI. PHASE-LOCKING FLOWS

The quasiperiodic and chaotic flows described in the previous section are not structurally stable, as we have surprisingly identified a rich variety of *resonant regions* where these flows generically recover time periodicities, that is, the flow undergoes a *phase-locking*. These regions, usually known as *Arnold tongues* or *horns*, are precisely born along the Neimark-Sacker bifurcation boundary (dark gray curve in Fig. 4). In this work, we have overall tracked four resonant regions within the parameter space (although many other may exist), namely $2:5$, $1:3$, $2:7$ and $1:4$, depicted in red, magenta, green and blue, respectively, in Fig. 4. These Arnold tongues are born at points A, B, C, and D whose (α, R) coordinates are enlisted in Table II. Mirror-symmetric resonant regions (reflected through the $\alpha = 5\pi/4$ line) also emerge from the points A′, B′, C′, and D′, whose coordinates can also be found in Table II. Inside those regions, the quasiperiodic orbits densely filling the stable torus, collapse into a periodic orbit on the torus, called a *phase-locked* flow. Dynamical systems theory predicts that, within the resonance region or horn, phase-locked periodic orbits come in pairs (Kuznetsov, 2004), one stable and the other unstable. This pair of periodic orbits are simultaneously created or annihilated at a saddle-node of cycles. The red, magenta, green, and blue colored curves appearing in Fig. 4 are precisely the loci of the saddle-node of phase-locked cycles, which are indeed the boundaries of the Arnold tongue regions. These curves have been computed by tracking (continuation) the phase-locked periodic orbits in parameter space using the PNK method described in section §III B. Although, in general, resonant regions tend to be supercritical (i.e., entirely contained above the Neimark-Sacker bifurcation boundary), our exploration reveals that some of them are mildly subcritical, as they slightly protrude below the Neimark-Sacker bifurcation boundary; see the cases $1:3$ or $1:4$ shown in Fig. 4, for example. That implies the possibility of hysteretical behavior resulting in oscillatory flows that may suddenly become phase-locked even before they become quasiperiodic. Left panels of Figs. 14a-d illustrate stable (nodal; solid black) and unstable (saddle; dashed gray) phase-locked periodic orbits within

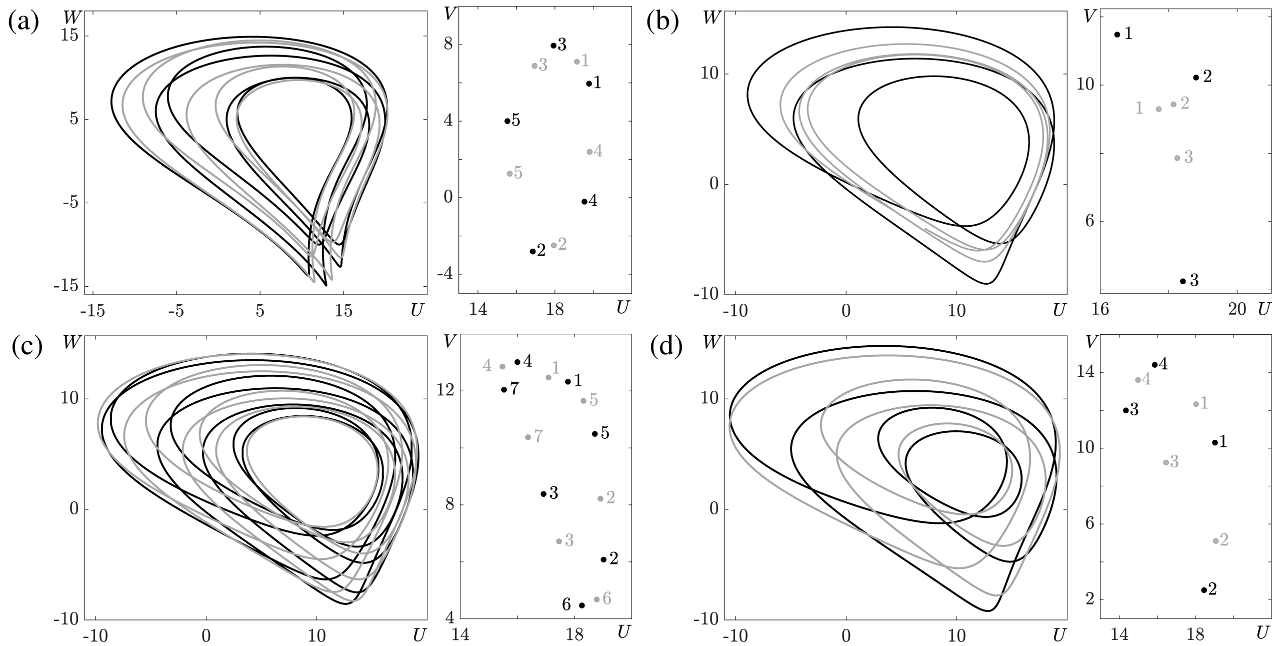

FIG. 14. $(U(t), W(t))$-phase portrait (left) and corresponding Poincaré section $W = 3$ (right) of phase-locked periodic orbits. Black (gray) indicating nodal-stable (saddle-unstable) solutions. (a) 2 : 5 at $(\alpha, R) = (5\pi/4, 31.4)$, (b) 1 : 3 at $(\alpha, R) = (4.08, 29.6)$, (c) 2 : 7 at $(\alpha, R) = (4.1, 29.2)$, (d) 1 : 4 at $(\alpha, R) = (4.12, 29)$.

the four identified resonant regions. The right panels show the Poincaré sections corresponding to these orbit pairs (i.e., fixed points of the Poincaré map), indicating the ordinality of the crossing sequences.

A detailed description of each one of the resonant regions is out of the scope of this work. However, we consider that the strong resonant case 1 : 4 deserves special attention, as it is one of the most challenging and not completely explored bifurcations found in dynamical systems theory. This case may lead to a large variety of bifurcation scenarios, depending on parameter values, some of which have been comprehensively scrutinized (Krauskopf, 1994; Wang, 1990). Figure 15 describes in detail the particular bifurcation scenario that has been identified in our exploration. In particular, Fig. 15a illustrates the parametric path ①-⑩ used to explore the flow regimes emerging within that resonant region. The Poincaré sections corresponding to these flow regimes are shown in panels (b) to (k). At point ①, the time-periodic flow is the only stable regime; red disk Fig. 15b. However, at point ②, slightly to the right of the saddle-node of cycles, and before crossing the Neimark-Sacker bifurcation boundary, a pair of phase-locked periodic orbits emerge; blue disks (focus-stable) and bullets (saddle-unstable) shown in Fig. 15c. In this case, the time-

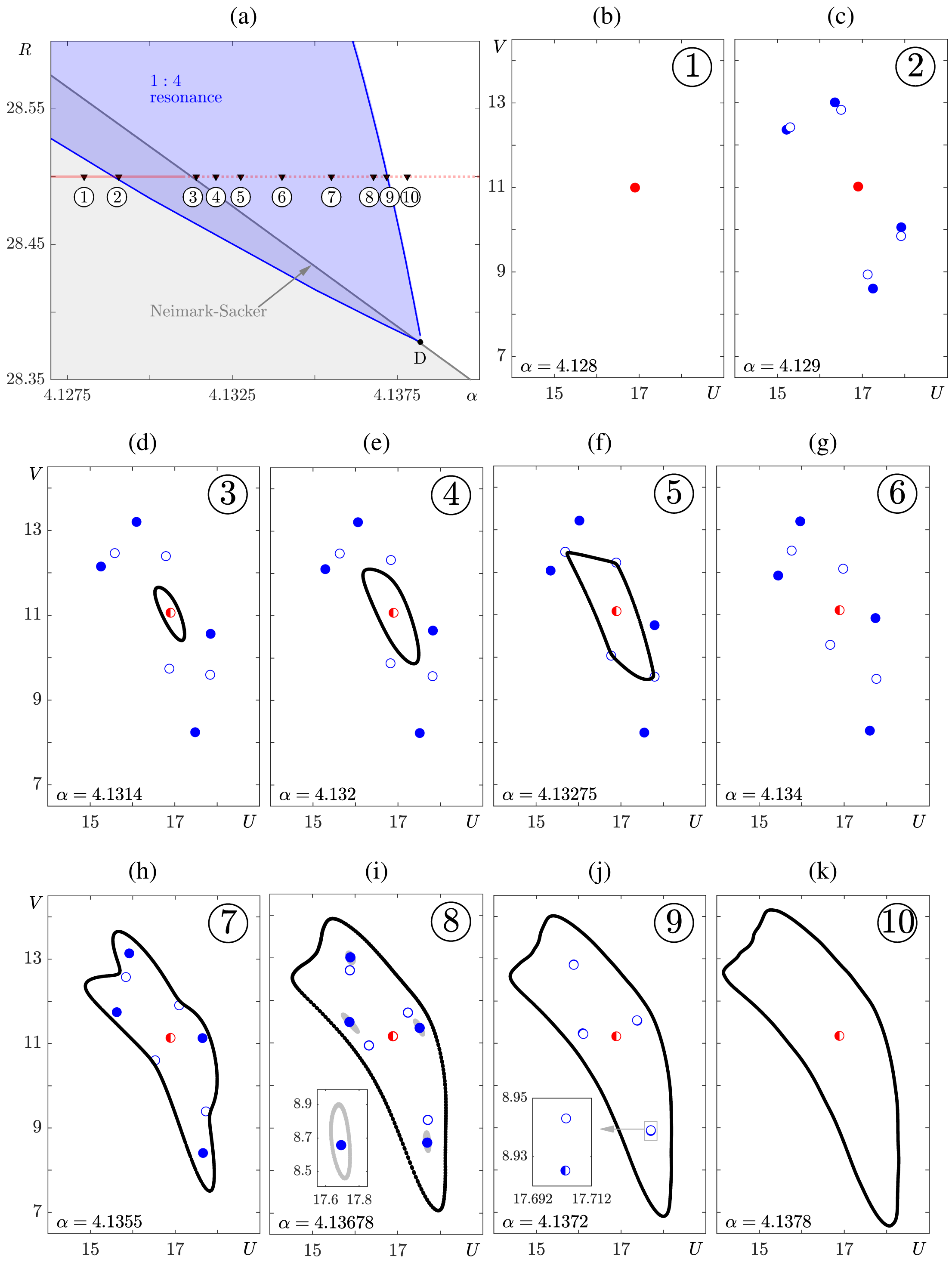

FIG. 15. Bifurcation sequence of time periodic (red), resonant phase-locked (blue), and quasiperiodic (black) flows, crossing the $1:4$ resonance region for $R = 28.5$. (a) Parametric path indicating different regimes along the sequence ①-⑩, whose (U,V)-Poincaré cross sections at $W = 3$ are shown in panels (b) to (k). Full (half) disks indicate stable (unstable; one complex conjugate pair of unstable Floquet eigenvalues) focus periodic flows, whereas bullets indicate saddle periodic orbits (one real unstable Floquet eigenvalue).

periodic flow is still linearly stable, coexisting with the other two phase-locked periodic orbits. The stable manifold of the unstable phase-locked orbit is the boundary between the basins of attraction of the two stable regimes. Figure 15d shows the phase portrait at point ③, just after the Neimark-Sacker bifurcation boundary has been crossed. The original periodic orbit is unstable (half red disk, denoting one pair of unstable complex conjugated eigenvalues), and a stable torus is born from it (closed black curve, encircling the unstable orbit). From points ④ to ⑤, this torus grows in size, collides with the saddle phase-locked orbit, and eventually disappears at a heteroclinic connection bifurcation, as shown in Figs. 15e-f. After the torus breakdown, the dynamics is governed by the phase-locked stable orbit; point ⑥ shown in Fig. 15g. However, at point ⑦, a large stable torus (black curve in Fig. 15h) appears through another homoclinic connection of the saddle phase-locked orbit. Whilst this outer stable torus grows in size, separating from the saddle orbit, an unstable torus appears from another homoclinic connection of the saddle orbit; in this case the tangency appears on the other side of the unstable manifold of the saddle. The unstable torus surrounds the linearly stable focus orbit (gray curve shown in the inset of Fig. 15i, depicting point ⑧ for $\alpha = 4.13678$). This unstable torus has been computed by means of the so-called *edge-tracking* technique (Skufca, Yorke, and Eckhardt, 2006), widely used in the computation of saddle Navier-Stokes solutions arising in shear flows. For slightly larger values of α, the unstable torus shrinks, eventually collapsing into the stable focus orbit, destabilizing it through a subcritical Neimark-Sacker bifurcation. Figure 16a shows the continuation of the upper and lower solution branches of $1:4$ phase-locked orbits along the resonance region, illustrating the aforementioned subcritical Neimark-Sacker bifurcation. The stable upper branch (focus, solid black curve) becomes unstable at point NS, close to the fold of phase locked orbit (white squares). The unstable torus, whose amplitude (relative to that of the phase-locked orbit) is qualitatively illustrated as a gray solid curve, emerges subcritically from the NS point, destabilizing the remaining part of the upper branch (dotted curve). Figure 16b depicts the cross-section of the iterated Poincaré map started from the two sides of the unstable manifold of the saddle orbit. Both iterations (red and orange points) eventually are attracted to the large outer torus (in black). To guide the eye, inset in Fig. 16b indicates the stable and unstable directions of the saddle, along with the unstable torus (gray curve) that acts as the edge state separating the basins of attraction of the stable phase-locked orbit and that of the outer stable torus. Fig. 15j depicts point ⑨, located immediately after the Neimark-Sacker bifurcation of the focus orbit (half blue disk shown in the inset), and slightly before the saddle-focus unstable orbits are about to collide at the fold of cycles, i.e., the boundary

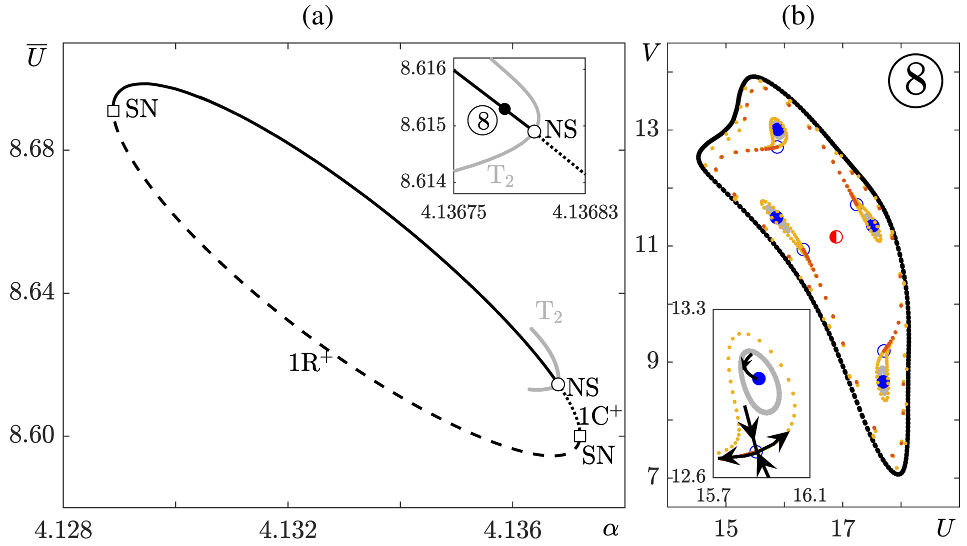

FIG. 16. Continuation and stability of upper and lower 1 : 4 phase-locked solution branches for $R = 28.5$. (a) Mean velocity $\overline{U} = T^{-1}\int_0^T U(t)\,\mathrm{d}t$ of the flows, with T being the corresponding period of the solutions. Solid and dashed linestyles indicate stability (focus) and instability (saddle, one real unstable eigenvalue; 1R$^+$), respectively. Dotted curve indicating unstable focus solution (a complex pair of unstable eigenvalues; 1C$^+$). Inset showing the stable orbit at ⑧ (black disk, to the left of the Neimark-Sacker bifurcation NS; black bullet), with leading eigenvalues $\lambda_1^{\pm} = 0.968 \pm 0.248\,\mathrm{i}$ of modulus $|\lambda_1^{\pm}| = 0.999$. White squares indicating the saddle-node (SN) or fold of cycles of the two solutions. (b) Poincaré map iterates (red and orange points) starting from the two sides of the unstable manifold of the saddle (blue bullet). Inset showing Poincaré map's flow orientations near the saddle and the unstable edge state torus.

of the resonance region. After that fold bifurcation, the two phase-locked periodic orbits disappear, the only remaining invariant sets being the unstable central periodic orbit (red half disk) and the outer stable torus (black curve); see Fig. 15k, illustrating point ⑩.

The family of phase portraits illustrated in Figs. 15(b-k) is consistent with those previously reported in dynamical systems theory (Krauskopf, 1994; Chow, Li, and Wang, 1994; Kuznetsov, 2004). In the aforementioned works, the analysis is based on a normal form derived for continuous dynamical systems, where the invariant sets are equilibria and periodic orbits. The present case, however, deals with the dynamics associated with the Poincaré map, so that equilibria (now fixed points of the first return map) must be replaced by periodic orbits, whilst the limit cycles are now represented by tori, i.e., invariant circles. Despite the different contexts, it can be concluded that the sequence of bifurcations ①-⑩ depicted in Figs. 15(b-k) perfectly matches with the scenarios described in the so-called *region VII* of the codimension-two parameter space, following the standard nomenclature used in Krauskopf (1994) or Kuznetsov (2004), as this is the only region where the periodic orbits may exhibit a subcritical Neimark-Sacker bifurcation (subcritical Hopf bifurcation of equilibria in the continuous case), as formally proved by Wang (1990).

VII. CONCLUSIONS

This work has comprehensively explored a wide variety of self-similar time-dependent flows (periodic, quasiperiodic, chaotic and phase-locked) arising between two infinite parallel plates that can independently stretch or shrink in orthogonal directions. For this particular problem, a rich diversity of exact Navier-Stokes steady solutions were already accurately computed in Ayats *et al.* (2021), covering an extensive range of Reynolds numbers, as well as all possible shrinking-stretching rates of the two plates. The present work is an extension of the previous paper, analyzing time dependent behaviours that were not considered in the previous analysis.

Exhaustive linear stability analyses provided here conclude that, among all the aforementioned flow families found in Ayats *et al.* (2021), the one that originates from the Stokesian approximation (solution branch A_1) is particularly relevant from a dynamical point of view, as it is the only stable solution of the Navier-Stokes problem, at least within the range of Reynolds numbers explored. The present study has therefore been focused on determining the fate of this particular type of flow, monitoring its stability and subsequent bifurcations that may lead to other time-dependent flows of dynamical relevance.

The A_1 solution branch is found to be linearly stable for low or even moderate Reynolds numbers. However, it is found that this flow destabilizes when both plates are shrinking at the same or comparable deceleration rates, leading to stable time-periodic flows that take over the dynamics after a Hopf bifurcation takes place. This is consistent with the oscillatory nature of flows reported in other wall-bounded problems in cartesian or cylindrical geometries with stretching or shrinking boundaries (Watson *et al.*, 1990; Marques *et al.*, 2017; Marques and Meseguer, 2019), even in the absence of the self-similarity assumption (Espín and Papageorgiou, 2009), and particularly when the boundaries are contracting. The resulting stable time-periodic flows identified have also been tracked with Poincaré-Newton-Krylov continuation techniques within the parameter space. When the two plates are shrinking at exactly the same deceleration rate, the oscillatory flows satisfy the so-called half-period shift and flip symmetry, as predicted by the equivariance of the equations and boundary conditions.

To predict ensuing bifurcations, the linear stability of these time-periodic flows has also been performed by computing their modulus-leading Floquet eigenvalues with an Arnoldi method. It is found that these oscillatory flows eventually become unstable by means of a Neimark-Sacker bifurcation that consequently leads to stable quasiperiodic regimes, where the phase space dynamics is confined to locally attracting tori. Sporadically, the quasiperiodic dynamics may be lost due to a Poincaré tangle mechanism that destroys the smoothness of the tori, so that the classical Ruelle-Takens-Newhouse route to chaos is at work, differing from the period-doubling cascades observed in Watson *et al.* (1990), Marques *et al.* (2017) or Espín and Papageorgiou (2009).

The most relevant finding here is that neither quasiperiodic nor chaotic flows are dominant. Surprisingly, both types of flows seem to systematically collapse with other periodic orbits, where the flow remains phase-locked and oscillatory again. This phenomenon is clearly ascribed to the emergence of multiple resonance regions, namely Arnold tongues or horns, that progressively populate the parameter space, above the Neimark-Sacker bifurcation boundary. Within these regions, the generic attractors are phase-locked periodic orbits. In the present study, up to four different resonance regions have been identified and their boundaries tracked. Of particular interest is the 1 : 4 strong resonance case, as it is one of the less explored codimension-two bifurcation scenarios in dynamical systems theory. In the present study, the 1 : 4 resonance region has been meticulously explored, and all the invariant sets (time-periodic or quasiperiodic flows - stable and unstable) within it, identified. The bifurcation sequences found in this exploration perfectly match the theoretical scenarios foreseen by normal form theory (Wang, 1990; Krauskopf, 1994).

ACKNOWLEDGMENTS

This work was supported by the Spanish MINECO grants No. FIS2017-85794-P and No. PRX18/00179, the Spanish MICINN grant No. PID2020-114043GB-I00, and the Generalitat de Catalunya grant No. 2017-SGR-785. BW's research was also supported by the Chinese Scholarship Council grant CSC No. 201806440152.

DATA AVAILABILITY

The data that support the findings of this study are available from the corresponding author upon reasonable request.

REFERENCES

Abraham, R. and Shaw, C. D., *Dynamics: The Geometry of Behavior*, 2nd ed., Studies in nonlinearity (Addison-Wesley, 1992).

Ayats, R., Marques, F., Meseguer, A., and Weidman, P., "Flows between orthogonally stretching parallel plates," Physics of Fluids **33**, 024103 (2021).

Ayats, R., Meseguer, A., and Mellibovsky, F., "Symmetry-breaking waves and space-time modulation mechanisms in two-dimensional plane Poiseuille flow," Physical Review Fluids **5**, 094401 (2020).

Aziz, T. and Mahomed, F. M., "Remark on classical Crane's solution of viscous flow past a stretching plate," Appl. Math. Lett. **52**, 205–211 (2016).

Brady, J. F. and Acrivos, A., "Steady flow in a channel or tube with an accelerating surface velocity. An exact solution to the Navier–Stokes equations with reverse flow," J. Fluid Mech. **112**, 127–150 (1981).

Chow, S.-N., Li, C., and Wang, D., *Normal forms and bifurcation of planar vector fields* (Cambridge University Press, 1994).

Crane, L. J., "Flow past a stretching plate," Zeitschrift für Angewandte Mathematik und Physik (ZAMP) **21**, 645–647 (1970).

Drazin, P. G. and Riley, N., *The Navier-Stokes Equations, A Classification of Flows and Exacts Solutions* (Cambridge University Press, Cambridge, 2006).

Espín, L. and Papageorgiou, D. T., "Flow in a channel with accelerating or decelerating wall velocity: A comparison between self-similar solutions and Navier-Stokes computations in finite domains," Phys. Fluids **21**, 113601 (2009).

Kelley, C., *Solving nonlinear equations with Newton's method* (SIAM, 2003).

Knoll, D. A. and Keyes, D. E., "Jacobian-free newton–krylov methods: a survey of approaches and applications," J. Comput. Phys. **193**, 357–397 (2004).

Krauskopf, B., "Bifurcation sequences at 1:4 resonance: an inventory," Nonlinearity **7** (1994).

Kuznetsov, Y. A., *Elements of Applied Bifurcation Theory*, 3rd ed. (Springer, 2004).

Marques, F. and Meseguer, A., "Extensional and torsional pipe flow," Physical Review Fluids **4**, 103908 (2019).

Marques, F., Meseguer, A., Mellibovsky, F., and Weidman, P., "Extensional channel flow revisited: a dynamical systems perspective," Proc. Roy. Soc. Lond. A **473**, 20170151 (2017).

Mellibovsky, F. and Meseguer, A., “A mechanism for streamwise localisation of nonlinear waves in shear flows,” J. Fluid Mech. **779**, R1–1 (2015).

Merkin, J. H. and Pop, I., “Stagnation point flow past a stretching/shrinking sheet driven by Arrhenius kinetics,” Appl. Math. Comput. **337**, 583–590 (2018).

Meseguer, A., *Fundamentals of Numerical Mathematics for Physicists and Engineers* (John Wiley & Sons, 2020).

Newhouse, S., Ruelle, D., and Takens, F., “Occurrence of strange axiom A attractors near quasi periodic flows on t^m, $m \geq 3$,” Commun. Math. Phys. **64**, 40 (1978).

Quarteroni, A., Sacco, R., and Saleri, F., *Numerical mathematics*, Vol. 37 (Springer Science & Business Media, 2010).

Skufca, J. D., Yorke, J. A., and Eckhardt, B., “Edge of chaos in a parallel shear flow,” PRL **96**, 174101 (2006).

Trefethen, L. N. and Bau, D., *Numerical Linear Algebra* (SIAM, Philadelphia, 1997).

Wang, C. Y., “The three-dimensional flow due to a stretching flat surface,” Phys. Fluids **27**, 1915 (1984).

Wang, C. Y., “Review of similarity stretching exact solutions of the Navier–Stokes equations,” Eur. J. Mechanics - B/Fluids **30**, 475–479 (2011).

Wang, D., “Hopf bifurcation at the nonzero foci in 1 : 4 resonance,” Acta Mathematica Sinica, New Series **6**, 10–17 (1990).

Waters, S. L., “Solute uptake through the walls of a pulsating channel,” J. Fluid Mech. **433**, 193–208 (2001).

Waters, S. L., “A mathematical model for the laser treatment of heart disease,” J. Biomech. **37**, 281–288 (2004).

Watson, E. B. B., Banks, W. H. H., Zaturska, M. B., and Drazin, P. G., “On transition to chaos in two-dimensional channel flow symmetrically driven by accelerating walls,” J. Fluid Mech. **212**, 451–485 (1990).

Weidman, P. and Ishak, A., “Multiple solutions of two-dimensional and three-dimensional flows induced by a stretching flat surface,” Communications in Nonlinear Science and Numerical Simulation **25**, 1–9 (2015).